

Modeling Effective Ionic Conductivity and Binder Influence in Composite Cathodes for All-Solid-State Batteries

Anja Bielefeld, Dominik A. Weber, and Jürgen Janek

ACS Appl. Mater. Interfaces, **Just Accepted Manuscript** • DOI: 10.1021/acsami.9b22788 • Publication Date (Web): 25 Feb 2020

Downloaded from pubs.acs.org on February 27, 2020

Just Accepted

“Just Accepted” manuscripts have been peer-reviewed and accepted for publication. They are posted online prior to technical editing, formatting for publication and author proofing. The American Chemical Society provides “Just Accepted” as a service to the research community to expedite the dissemination of scientific material as soon as possible after acceptance. “Just Accepted” manuscripts appear in full in PDF format accompanied by an HTML abstract. “Just Accepted” manuscripts have been fully peer reviewed, but should not be considered the official version of record. They are citable by the Digital Object Identifier (DOI®). “Just Accepted” is an optional service offered to authors. Therefore, the “Just Accepted” Web site may not include all articles that will be published in the journal. After a manuscript is technically edited and formatted, it will be removed from the “Just Accepted” Web site and published as an ASAP article. Note that technical editing may introduce minor changes to the manuscript text and/or graphics which could affect content, and all legal disclaimers and ethical guidelines that apply to the journal pertain. ACS cannot be held responsible for errors or consequences arising from the use of information contained in these “Just Accepted” manuscripts.

Modeling Effective Ionic Conductivity and Binder Influence in Composite Cathodes for All-Solid-State Batteries

Anja Bielefeld,^{*,†,‡} Dominik A. Weber,[‡] and Jürgen Janek^{*,†,¶}

[†]*Physikalisch-Chemisches Institut, Justus-Liebig-Universität, 35392 Giessen, Germany*

[‡]*Volkswagen AG, Group Research, 38436 Wolfsburg, Germany*

[¶]*Center of Materials Research (LaMa), Justus-Liebig-Universität, 35392 Giessen, Germany*

E-mail: anja.bielefeld@volkswagen.de; juergen.janek@phys.chemie.uni-giessen.de

Abstract

In the pursuit for future mobility, solid-state batteries open a wide field of promising battery concepts with a variety of advantages, ranging from energy density to power capability. However, trade-offs need to be addressed, especially for large-scale, cost-effective processing, which implies the use of polymeric binder in the composite electrodes. Here, we investigate three-dimensional microstructure models of active material, solid electrolyte and binder to link cathode design and binder content with electrode performance. Focusing on lithium ion transport, we evaluate the effective ionic conductivity and tortuosity in a flux-based simulation. Therein, we address the influence of electrode composition and active material particle size as well as the process-controlled design parameters of void space and binder content. Even though added in small amounts, the latter has a strong negative influence on the ion transport paths and the active surface area. The simulation of ion transport within four-phase

composites is supplemented by an estimation of the limiting current densities - illustrating that application-driven cell design starts at the microstructure level.

Keywords

all-solid-state batteries, cathode composite, percolation, NCM materials, polymer binder

1 Introduction

Paving the way towards e-mobility, high-energy battery cells, produced on a large-scale, are highly sought-after. While conventional Li-ion battery technology and its processing is well-established¹, it is also about to hit its physico-chemical limits² and all-solid-state batteries (ASSBs) are widely treated as jack of all trades in battery technology. They offer the potential to outperform conventional technology in terms of energy density, charging and power capability³ at a wide thermal stability window⁴, but a major issue yet to be resolved is cost-effective upscaling⁵.

When enabling the lithium metal anode, ASSBs hold promise to reach ambitious energy density targets, albeit a dense, thin and dendrite-safe solid electrolyte (SE) separator layer remains yet to be realized.⁶ Reconciliation with the aforementioned goals is what poses major challenges in ASSB research on various levels: On the material level, solid electrolytes are still driven towards higher conductivities⁷ and wider electrochemical windows⁸, with adequate tuning of interfaces^{9,10} and interphases¹¹ gaining importance, as they strongly influence cell performance. The controversial discussion on space charge layers¹²⁻¹⁴ goes along with degradation prevention by particle coatings on the cathode side^{10,15-19} and the introduction of sacrificial layers on Li-metal anodes²⁰. On the cell level, the electrode design, especially on the cathode side, can be crucial for cell performance and has to be designed according to the use case of the cell: particle morphologies, sizes and their distributions as well as residual voids influence percolation behavior, thereby affecting ionic and electronic conduction

and the active surface area, available for Li-insertion^{21–28}. Furthermore, volume change of cathode active material particles may lead to contact loss upon cycling^{29,30}, and therefore influences performance, as well. When it comes to processing ASSB cells cost-efficiently, upscaling for industrial application⁵ is crux of the matter. Accordingly, processing of materials and composites in a wet slurry-based fabrication, comparable to state-of-the-art Li-ion technology would be favorable, but requires the incorporation of binder which has negative impact on cell performance^{15,25,31–34}.

The role of binder, apart from enabling a high-throughput roll-to-roll process, is to act as a buffer for mechanical strain, induced upon cycling by the volume change of active material particles and to prevent peel-off and brittleness of the electrodes³¹. While the volume change of LiCoO₂ (LCO) is limited to around 2 vol% expansion upon cell charging, LiNi_xCo_yMn_zO₂ (NCM) shrinks by up to 6 vol% when delithiated for nickel-rich NCM811, in particular³⁰. Apart from the mechanical issue, solid electrolytes pose challenges for a suitable binder choice as well: Thiophosphate solid electrolytes show high reactivity with polar solvents^{35,36}. Therefore, the trade-off between solubility in a non- or less polar solvent and sufficient binding ability for compensation of volume changes has to be resolved^{25,31,35}. Due to the solubility in less polar solvents, such as xylene or toluene, many studies focus on nitrile butadiene rubber (NBR)^{15,25,35,37} or styrene butadiene rubber (SBR)³³ as binder. In comparison, dry-processed binder-free electrodes outperform wet-processed electrodes²⁵, because most binders are ionic and electronic insulators that block active surface area needed for Li-insertion and impede ionic and electronic pathways through the composite. Furthermore, wettability, homogeneity and processability, mainly depending on viscosity, have to be considered, as well³⁸. One approach to avoid the aforementioned issues and to maintain rate performance similar to dry-processed electrodes, is minimizing the binder amount. Hippauf et al.³² manufactured NCM955 and Li₆PS₅Cl (LPSCl) electrode sheets in a solvent-free process with down to 0.1 wt% polytetrafluoroethylene (PTFE) binder, which is assumed to have fibril morphology. Another approach is to remove the binder from the readily formed electrode by heat

treatment as performed by Yamamoto et al.³⁴, who use volatile poly(propylene carbonate)-based binder (PPC) in NCM111 and β -Li₃PS₄ (LPS) composites. The binder undergoes thermal depolymerization by unzipping, evaporates at temperatures above 300 °C and does not impede conduction afterwards. Oh et al.³¹ suggest the introduction of a lithium ion-conducting ionic liquid, Li(G3)TFSI (G3: triethylene glycol dimethyl ether, LiTFSI: lithium bis(trifluoromethanesulfonyl)imide), into NBR in NCM622 and NCM711 cathodes with LP-SCI electrolyte for sufficient ionic pathways and contact, achieving enhanced performance compared to pure NBR and enabling quite high cathode thicknesses of 200 μ m.

In this work, we address processing and cell design issues for composite cathodes based on thiophosphate solid electrolytes and NCM active material from a modeling perspective. We shed light on effective ionic conductivity, the associated tortuosity of composite electrodes and their dependence on cell design parameters, such as active material (AM) particle size and size distribution, composition, void space and binder content. Based on the effective conductivity and a couple of basic assumptions, we estimate maximum current densities achievable with these cathodes, judging the impact that microstructural electrode layout and its modifications can have in ASSBs.

2 Methods

The starting point for this work was our recently published conduction cluster analysis and percolation study²¹. Therein, electronic and ionic percolation of computed two-component ASSB cathode microstructures was evaluated: Particle arrangements consisting of AM and SE particles were generated in GeoDict³⁹ in a rectangular parallelepiped of voxels, where the voxel length is associated with the microstructure's resolution. In order to reconstruct realistic composites of NCM and thiophosphate SE, the AM was represented by spherical, non-overlapping secondary particles. The introduction of single crystal NMC in the model microstructures would imply moving to more complex particle shapes. However, anisotropic

ion transport in these particles would not have to be taken into account, for the effective ionic conductivity, as the ionic conductivity of the solid electrolyte is four orders of magnitude higher than in the NMC (see assumption 2 below). The morphology of the SE particles was emulated by convex polyhedra that were allowed to exhibit overlap, to take account for the relatively low Young's modulus of ~ 25 GPa of thiophosphates^{40,41}, which reflects the materials' good ductility.

Two basic assumptions were made to compute the conductive networks: 1) The SE is a single-ion conductor with negligible electronic conductivity. 2) The AM's ionic conductivity is four orders of magnitude smaller than its SE equivalent and can therefore be neglected. Interconnected neighboring particles were considered to form a conduction cluster, so ionic conduction clusters consisted of connected SE particles and electronic conduction clusters were formed by connected AM particles, while no carbon additives were introduced. The material fraction that belongs to the conduction cluster, was then referred to as the utilization level. For the AM, the utilization level can be seen as an equivalent to the accessible electrode capacity, because isolated AM particles cannot be addressed upon cycling. Combined with the active interface area between the conduction clusters, the utilization level provides a hint on electronic or ionic limitations in the microstructure properties, even though this network analysis does not contain information on diffusion lengths and the tortuosity of ionic or electronic pathways.

The model microstructures in our previous work can be associated with pressed lab cells, which are based on carbon-free and binder-free composites. In this work, we target at modeling electrodes manufactured in a casting process: We suppose that electronic conduction is not the limiting factor, because conductive carbon will be introduced into ASSB electrodes on their way to commercialization. A recent analysis of solid state systems by Randau et al.⁴² indicates that many studies already do so and our focus therefore lies on ionic conduction. Furthermore, we study the influence of binder and go beyond the computation of utilization levels and active interface areas by calculating effective properties. However, the study on

the active material size, the void space and the electrode composition are not restricted to electrodes manufactured in a casting process.

2.1 Tortuosity

In cells with liquid electrolyte, two properties are used to characterize ion diffusion within the liquid electrolyte in porous electrodes at a continuum level: porosity ϵ and tortuosity τ (or the tortuosity factor $\kappa = \tau^2$). The porosity ϵ is defined as the volume fraction available for the fluid, or correspondingly, as the volume fraction, not filled with the solid matrix. Tortuosity τ accounts for the tortuous and curvy trajectory the dissolved ions have to follow, passing through the porous volume. In homogenizing the complex microstructure, its effective diffusion coefficient $D_{\text{eff}}^{\text{ion}}$ is then given by

$$D_{\text{eff}}^{\text{ion}} = \frac{\epsilon}{\tau^2} D_{\text{bulk}}^{\text{ion}} = \frac{\epsilon}{\kappa} D_{\text{bulk}}^{\text{ion}}, \quad (1)$$

where $D_{\text{bulk}}^{\text{ion}}$ represents the ion diffusion coefficient of the bulk material.

Even though there is no fluid involved in ASSBs and the prevailing transport mechanism is ionic migration rather than diffusion, it is common to transfer the description of fluids to ASSB electrodes. On the assumption that interactions between lithium ions and lattice vacancies in the SE can be neglected⁴³, the Nernst-Einstein equation can be used to link the lithium diffusion coefficient $D_{\text{bulk,SE}}^{\text{ion}}$ and the ionic bulk conductivity of the SE $\sigma_{\text{bulk,SE}}^{\text{ion}}$

$$D_{\text{bulk,SE}}^{\text{ion}} = \frac{\sigma_{\text{bulk,SE}}^{\text{ion}} RT}{c_{\text{bulk,SE}}^{\text{ion}} F^2}. \quad (2)$$

Ionic conduction in the (now) solid electrolyte is tortuous as well and the effective conductivity $\sigma_{\text{eff}}^{\text{ion}}$ may differ significantly from the bulk conductivity⁴⁴:

$$\sigma_{\text{eff}}^{\text{ion}} = \frac{\epsilon_{\text{SE}}}{\tau^2} \sigma_{\text{bulk,SE}}^{\text{ion}}. \quad (3)$$

The gentle reader may keep in mind that the term porosity can be ambiguous for ASSB electrodes, as it is also used for the volume fraction which is not filled by any electrode component^{21,26,35}. In the composite microstructures, we therefore distinguish between the void space ϕ , the total volume fraction of the SE with respect to the entire electrode volume (including void space ϕ) ϵ_{SE} and the SE volume fraction related to the solid electrode volume ν_{SE} which are correlated by $\epsilon_{\text{SE}} = (1 - \phi)\nu_{\text{SE}}$.

Geometrically, tortuosity is defined as the shortest pathway Δl through the microstructure scaled by its length Δx ⁴⁵

$$\tau = \frac{\Delta l}{\Delta x}. \quad (4)$$

However, this tortuosity only accounts for the shortest pathway and does not average with wider, but longer pathways which are also used by the fluid and have influence on effective diffusion. The geometrical tortuosity therefore underestimates the tortuosity compared to experiment-based values or flux-based simulations⁴⁵.

To determine the tortuosity of electrode samples practically, bulk and effective properties can be measured and compared according to Equation 1^{27,44}, or (for conventional cells) electrochemical impedance spectroscopy is used in a symmetric cell setup with an electrolyte salt that does not contain lithium and therefore inhibits lithium insertion, to achieve information on the tortuosity^{46,47}. Furthermore, 3D reconstruction of X-ray tomography data⁴⁸ or focused ion beam-scanning electron microscopy data (FIB-SEM)⁴⁹ may be used. To extract tortuosity from tomography data, either geometry-based or flux-based calculations are applied⁴⁵. Because of the above-mentioned issues with the geometry-based method, we simulate the effective ionic conductivity $\sigma_{\text{eff, ion}}$ in a flux-based approach and calculate the tortuosity according to Equation 3, but for ionic conductivity.

We further want to point out that both systems, liquid and solid, hold complications that are not considered in this continuum description: In liquid systems, adsorption and space charge affect charge transport, while grain boundary diffusion is an issue in solid systems.

2.2 Flux-based calculation of effective conductivity

The calculation of the effective conductivity is a problem of a complex composite consisting of multiple phases with different conductivities. Hence, the effective conductivity σ_{eff} of a 3-dimensional microstructure is a symmetrical second order 3x3-tensor. Since conduction in ASSB cathodes is essentially taking place perpendicular to the current collector plane, which we define as the x_3 -direction, it is sufficient to compute the diagonal term σ_{33} and its off-diagonal neighbors σ_{13}, σ_{23} , that indicate the tendency of ions to deviate in the x_1 and x_2 -direction, during their predominant motion in the x_3 -direction. The tensor then takes the form

$$\sigma_{\text{eff}} = \begin{pmatrix} \sigma_{11} & \sigma_{12} & \sigma_{13} \\ \sigma_{21} & \sigma_{22} & \sigma_{23} \\ \sigma_{31} & \sigma_{32} & \sigma_{33} \end{pmatrix} = \begin{pmatrix} - & - & \sigma_{13} \\ - & - & \sigma_{23} \\ - & - & \sigma_{33} \end{pmatrix}. \quad (5)$$

The common approach in GeoDict³⁹ is to describe electrical conduction, or charge transport in general, analogous to heat conduction, as the governing mathematical equations for these processes are of the same kind. Therefore a solver for the stationary heat equation

$$\nabla \cdot (\beta \nabla T) = f \text{ in } \Omega, \quad (6)$$

developed by Wiegmann and Zemitis⁵⁰, is used, with the local conductivity $\beta(\mathbf{x})$, the temperature T and heat sources or sinks f in the model volume $\Omega = (0, l_1) \times (0, l_2) \times (0, l_3)$. Under the assumption, that each voxel's properties are known and that the interfaces of two materials are defined by the voxel faces, the so-called EJ-heat solver uses harmonic averaging and introduces explicit jumps across materials interfaces to solve for the effective conductivity tensor⁵⁰.

For ionic conductivity, Ohm's law

$$\mathbf{j} = \sigma \mathbf{E} = -\sigma \nabla \varphi \tag{7}$$

links the current density \mathbf{j} to the gradient of the electric potential φ and the ionic conductivity σ . The electric field is referred to as \mathbf{E} . In the stationary case, the continuity equation for charge

$$\frac{\partial \rho}{\partial t} + \nabla \cdot \mathbf{j} = 0, \tag{8}$$

with the charge density ρ , becomes

$$\nabla \cdot \mathbf{j} = 0 \tag{9}$$

$$\nabla \cdot (-\sigma \nabla \varphi) = 0 \tag{10}$$

and therefore takes the form of a Poisson equation analogous to the stationary heat equation 6, that can be solved by applying a potential difference on both sides of the microstructure as boundary condition. Different from our percolation study²¹, an ionic conductivity is assigned to both components (see Table S1, Supporting Information), where the ionic conductivity of the AM (here NCM532, measured by Amin and Chiang⁵¹) is four order of magnitude smaller than that for the SE. As the contact resistance between the two components, we take the value of 40 $\Omega \text{ cm}^2$ estimated by Braun et al.⁵² from EIS and SEM data of Kato et al.⁴.

Since the effective ionic conductivity is provided by the simulation, the ionic tortuosity factor has finally been calculated as

$$\tau^2 = \frac{\sigma_{\text{bulk,SE}}^{\text{ion}}}{\sigma_{\text{eff}}^{\text{ion}}} \epsilon_{\text{SE}}. \tag{11}$$

2.3 Incorporation of binder

Concerning microstructure reconstruction based on FIB-SEM or X-ray tomography and modeling, the presence of binder, as well as conductive carbon, poses challenges: While the size of AM and SE particles are on the micrometer scale, the size of binder molecules and conductive carbon particles are rather on the nanoscale^{53,54} requiring either a combination of imaging methods or appropriate resolution, thereby still ensuring a representative volume⁴⁹. Moreover, the distinction of the solid phases in the images is non-trivial, as sufficient contrast is required⁴⁹. Therefore, there is a lack of knowledge on the distribution of binder in battery electrodes. The morphology of the carbon-binder conductive (CBC) network is not well-known, strongly dependent on processing and can have significant influence on effective properties. Nanoporosity of the CBC network can amplify the effect of surface coverage by binder and lead to reduced active interface area⁴⁸.

Moreover, binders can exhibit quite different characteristics, depending on the functionality they are tailored to, with wettability, mechanical stability, resistivity, density and morphology³⁸ as factors that have not yet been accounted for in microstructural modeling. Our approach is to set up a model where the binder does not exhibit a specific morphology (such as e.g. PTFE, which takes the shape of fibrils) on the micro-scale, but preferably smears up voids between AM particles. Accordingly, the binder covers active interface area and may affect ionic transport throughout the cathode, as observed previously²⁵.

We use the AM microstructures generated in our previous work²¹ and add the binder according to the procedure in GeoDict³⁹, which targets the shape of a concave meniscus in locations where surfaces come close together. The process is explained and illustrated in the Supporting Information (Figure S1 and S2).

2.4 Estimation of current densities

When current is applied to an electrode, internal resistance will cause a voltage drop over the composite. To quantitatively judge the role of effective ionic conductivity and microstructure,

we estimate the current density through a composite electrode and its associated C-rate that evolves from the electrode design, material-inherent parameters and the voltage drop (also known as IR drop). The approach is schematically shown in Figure S3, Supporting Information. Similar to Kato et al.⁴⁴, we assume that the potential drop originates from ionic conduction, while electronic transport is not limiting due to the presence of conductive carbon. Furthermore, we neglect all non-Ohmic behavior such as charge-transfer effects or ionic diffusion in the AM. Accordingly, the scalar current density j can be calculated by Ohm's law

$$j^{\text{ion}} = \frac{I^{\text{ion}}}{A} = \frac{\Delta U}{R^{\text{ion}} A} \quad (12)$$

with the given voltage drop ΔU , the electrode surface area A and the electrode resistance R^{ion} that, when expressed in terms of the specific resistance $\rho_{\text{eff}}^{\text{ion}}$, is dependent on the electrode thickness l

$$\rho_{\text{eff}}^{\text{ion}} = \frac{1}{\sigma_{\text{eff}}^{\text{ion}}} = R^{\text{ion}} \frac{A}{l}. \quad (13)$$

Insertion of the effective ionic conductivity in Equation 3, then allows to estimate the current density as

$$j^{\text{ion}} = \sigma_{\text{bulk, SE}}^{\text{ion}} \frac{\epsilon_{\text{SE}}}{\tau^2} \frac{\Delta U}{l}, \quad (14)$$

$$= \sigma_{\text{bulk, SE}}^{\text{ion}} \frac{v_{\text{SE}} \cdot (1 - \phi)}{\tau^2} \frac{\Delta U}{l}, \quad (15)$$

The associated C-rate can then be calculated for a chosen AM with the specific capacity c_{AM} , density ρ_{AM} and solid volume fraction v_{AM} .

$$C = \frac{j^{\text{ion}}}{c_{AM} \rho_{AM} v_{AM} (1 - \phi) l}, \quad (16)$$

$$= \frac{\sigma_{\text{bulk, SE}}^{\text{ion}}}{c_{AM} \rho_{AM} \tau^2} \frac{v_{SE}}{v_{AM}} \frac{\Delta U}{l^2}. \quad (17)$$

Analog to the solid electrolyte volume fractions ν_{SE} and ϵ_{SE} , the AM volume fraction referring to the solid volume is denoted as v_{AM} and related to the AM total volume fraction ϵ_{AM} by $\epsilon_{AM} = \nu_{AM}(1 - \phi)$.

3 Results and discussion

3.1 Effective conduction

Sufficient effective ionic conductivity is essential for power capability and fast charging. We therefore study the ionic conduction properties for a variety of model microstructures. If not indicated otherwise, a void space of 15 % in the particle arrangements is chosen. The data availability on void space is sparse, but we are confident that our choice is a reasonable compromise for slurry-based electrodes, which are reported to possess 20-30 % residual porosity in an uncalendered state⁵⁵, as well as pressed electrodes with 13.2 % residual porosity²⁶. Infiltration of LPSCl into conventional LCO and graphite electrodes followed by cold-pressing is reported to decrease the void space to 6-8 %³⁵.

3.1.1 Comparison with the literature

In order to validate that we are indeed capable of reproducing practically obtained effective properties with our microstructures, we reconstructed a LCO:Li₁₀GeP₂S₁₂ (LGPS):Acetylene Black cathode microstructure based on a cross-sectional SEM image from Kato et al.⁴⁴. Figure S4, Supporting Information, shows the SEM image and a cross-section of our recon-

struction. Since LCO does not exhibit spherical morphology like NCM, we modeled the AM as five-edged planar polyhedra and assumed Gaussian distributions for the particle thickness l_{AM} and ray length r_{AM} , which is defined as the distance from the polyhedron center to the outer face center. Unfortunately, no information on void space in the pressed electrode is provided and the SEM image does not allow to distinguish between acetylene black and void space. As the residual void space is an important electrode characteristic, we assumed 15 % for our model, similar to the measured void space from Hlushkou et al.²⁶. An overview of the model parameters is provided in Table S2, Supporting Information.

In the flux-based simulation, we get an effective ionic conductivity of 0.68 mS cm^{-1} with an associated ionic tortuosity factor of 2.29, while Kato et al.⁴⁴ report 0.73 mS cm^{-1} and 2.47, respectively. The reader should be aware that the calculation of the tortuosity factor is ambiguous, because Kato et al.⁴⁴ do not account for the residual void space, which is undoubtedly not absent in a pressed electrode. The SE volume fraction ϵ_{SE} in Equation 11 should not ignore the voids and therefore be calculated as $\epsilon_{SE} = (1 - \phi)\nu_{SE}$, which reduces the tortuosity value slightly. Still, the effective properties of the reconstructed microstructure are in good accordance with the experimental values and confirm the potential of the flux-based simulation approach.

3.1.2 AM particle size

To date, the impact of AM particle size in ASSB composite electrodes is not intuitive: On the one hand, previous work shows that the conduction networks are affected by AM particle size with small AM diameters leading to enhanced electronic percolation²³ and increased active surface area²¹, on the other hand, Froboese et al.²⁷ reported the tendency of high ionic tortuosity for small particles in their experimental model study on electrochemically inert glass particles in a composite with polymer SE and Shi et al.²⁸ recommend a high AM/SE particle size ratio for enhanced ionic percolation properties. This indicates a possible trade-off between electronic and ionic conduction, connected with the choice of particle size for

the AM. We therefore computed the effective ionic conductivity for uniform AM particle diameters between 3 μm and 15 μm , as these are typical sizes available for NCM secondary particles^{56,57}. In order to avoid potential bias by the choice of the distribution settings, we chose to keep the parameter space smallest possible and to model uniform particle sizes. An extension to multimodal size distributions follows thereafter. Figure 1a shows that the effective ionic conductivity does not only strongly depend on the electrode composition, but is also influenced by AM particle size: An increasing AM fraction, which is needed for high energy application, linearly reduces the effective ionic conductivity for all particle sizes. Beyond that, smaller AM particles lead to reduced effective conductivity, as well. This behavior can also be observed in the ionic tortuosity factor in Figure 1b which starts at $\tau^2 \simeq 2$ for an AM to SE volume ratio of 50:50 and rises monotonously at a close-to linear slope until 65:35 AM:SE. In this region, the tortuosity factors are in the range of $\tau^2 \in [2, 5]$ and therefore similar to those observed in conventional NCM cathodes^{46,47,58}. Above a volume ratio of 65:35 AM:SE, the ionic tortuosity rises abruptly, especially for small particle sizes. This tendency is also reported by Froboese et al.²⁷, who explain that small AM particles lead to a higher total amount of particles in the structure that act as obstacles for bypassing ions. In a joint model and experimental study on NMC:LPS-composites, Shi et al.²⁸ show that increasing the AM/SE particle size ratio is favorable for ionic percolation networks and becomes particularly important for high AM loading, where ionic percolation is critical. Our results are in accordance, as we model the SE at a fixed particle size of 3 μm and find enhanced ionic conductivity for increased AM particle size, which is equivalent with a high AM/SE particle size ratio. In general, pore size scales with particle size⁵⁹, which means that smaller AM particles may offer more ionic pathways. On the other hand these pathways are narrow and do not allow for ionic currents as high as with the wider pathways in composites with coarse particles.

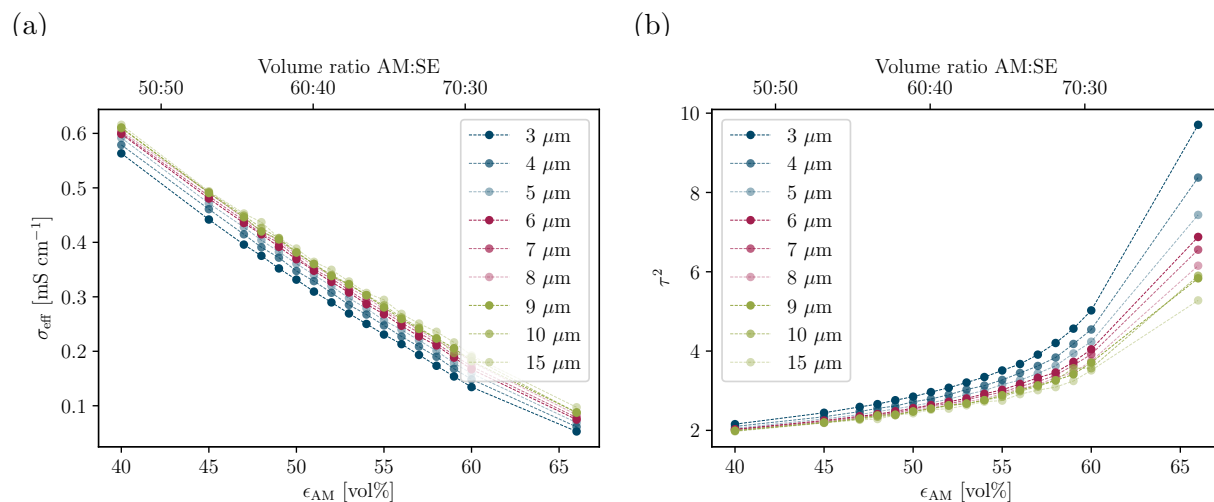


Figure 1: (a) Effective ionic conductivity and (b) ionic tortuosity factor of composite microstructures vs. composition for uniformly distributed AM; particle sizes between $d \in [3, 15] \mu\text{m}$; electrode void space held constant at $\phi = 15\%$.

3.1.3 Comparison with the Bruggeman relation

The Bruggeman relation is commonly used to calculate the tortuosity factor for battery electrodes or to compare it to measured values. Therefore, it is worthwhile to judge its applicability to our model system. The Bruggeman relation itself is a mathematically derived equation for a porous medium of spherical particles in an ideal homogeneous distribution⁶⁰, describing the ionic tortuosity factor solely with regard to the porosity

$$\tau^2(\epsilon) = \epsilon^{-\frac{1}{2}}. \quad (18)$$

Due to the constraints in the underlying assumptions, a wide variety of modifications has been applied to the Bruggeman equation for more complex structures⁶¹. In the context of battery electrodes, an additional factor γ and the use of the exponent α as a fit parameter is common^{27,45,47,62}, resulting in the modified Bruggeman equation

$$\tau^2(\epsilon) = \gamma \epsilon^{-\alpha}. \quad (19)$$

Naturally, the modified Bruggeman equation 19 describes data more accurately than Equation 18, because it incorporates two additional degrees of freedom within the fit parameters α and γ . For $\alpha = 0.5$ and $\gamma = 1$, the modified equation reduces to the original Bruggeman equation.

To compare the flux-based computed tortuosity factors of this work with the Bruggeman equation(s), we chose to take a closer look at the minimal and maximal particle size, since the tortuosity factors of all other AM particle sizes lie in between. Figure 2 shows the ionic tortuosity factor's dependence on the total fraction of SE $\epsilon_{\text{SE}} = (1 - \phi) \cdot \nu_{\text{SE}}$ in context with the Bruggeman equation 18 and the modified/fitted Bruggeman equation 19. Clearly and similar to studies on conventional battery electrodes^{47,49}, the Bruggeman equation significantly underestimates the tortuosity factor and does not adequately describe the complexity of electrode microstructures. The mismatch is pronounced especially for small AM particles and small SE fractions, where the values of the model microstructures are 4-fold larger than the Bruggeman equation 18 predicts. The modified Bruggeman equation 19 describes the behavior acceptably, but incorporates parameters of $\alpha \in [2.02, 1.21]$ and $\gamma \in [0.32, 0.67]$, which are far off from 0.5 and 1, but similar to the ones found by Froboese et al.²⁷. In our opinion, these parameters do not offer any further scientific insight. In contrast to conventional electrodes, further characteristics like the morphology, particle size and distribution of the SE particles in ASSB electrodes can affect ionic tortuosity. These properties are not taken into account in the Bruggeman equation(s), making it even less applicable for ASSB cathodes than for conventional cathodes.

3.1.4 Multimodal AM particle size distributions

The idea of multimodal size distributions is to improve densification, since the limit for dense packing of equally sized spheres at 74 %⁶³ does not apply. In particular, both the hexagonal and the cubic close-packing of equally sized spheres r_L contain octahedral and tetrahedral voids, which can be filled with medium-sized spheres of radius $r_M = (\sqrt{2} - 1)r_L$ and small

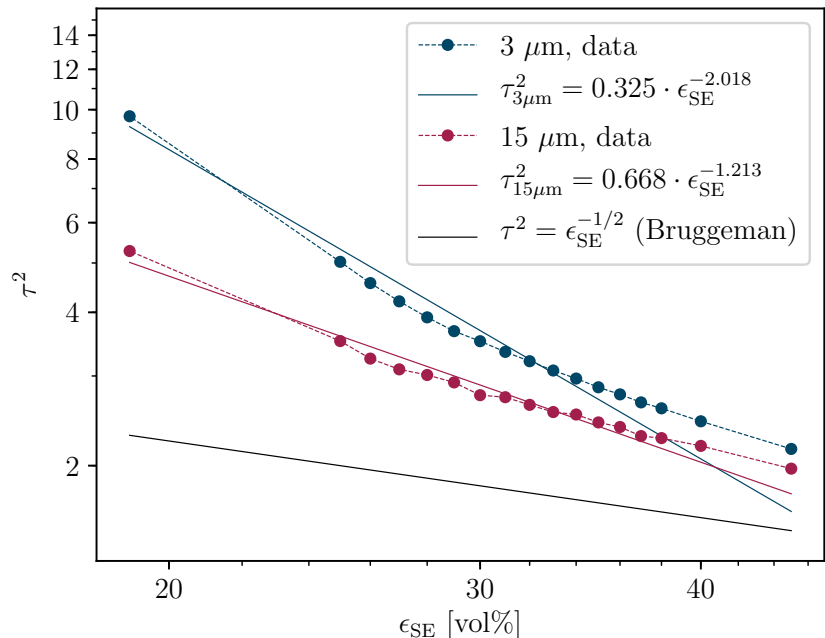


Figure 2: Simulated ionic tortuosity factor and comparison with the Bruggeman equation 18 and the modified Bruggeman equation 19 for composite microstructures vs. total fraction of SE; uniformly distributed AM at particle size $d = \{3, 15\} \mu m$; electrode void space held constant at $\phi = 15 \%$.

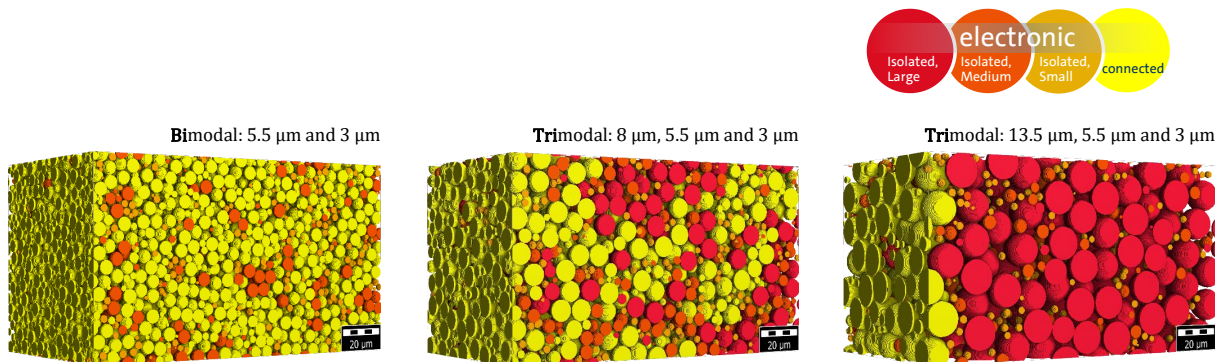
spheres with $r_S = \left(\sqrt{\frac{3}{2}} - 1\right) r_L$. For ideal packing with n large spheres (L) with radius r_L , $2n$ small spheres (S) with radius r_S are needed to fill the tetrahedral voids and n medium spheres (M) with radius r_M are necessary to fill the octahedral voids⁶⁴. We therefore focused on trimodal distributions with a number ratio of 1:1:2 for L:M:S and used the above mentioned ideal size distribution with $d_S = 2 \cdot r_S = 3 \mu m$ as the lower limit for secondary NCM particles. Accordingly, the medium-sized particles were $5.5 \mu m$ in size and the associated large particle size was $13.3 \mu m$. The effect of particle size was then studied by variation of the large particle size within $d_L \in [5.5, 13.5] \mu m$, so that the distribution became bimodal in the lower limit of $5.5 \mu m$, as illustrated in Figure 3a.

Figure 3b and 3c show that also in multimodal distributions, arrangements of smaller particles result in reduced effective ionic conduction and higher tortuosity for multimodal distributions. The effect of particle size on tortuosity is observable in regions where ionic conduction

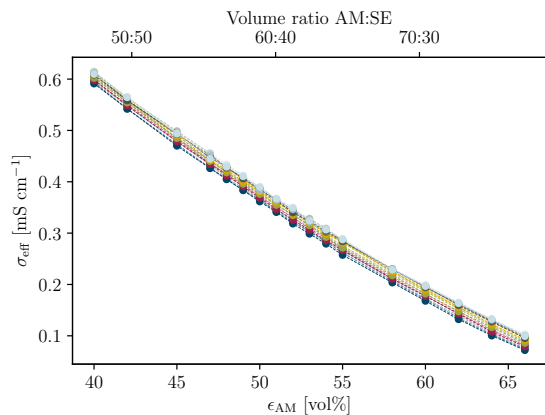
becomes limiting and high energy density is achieved due to a large AM fraction. Compared to monomodal particle arrangements, the tortuosity is generally lower, even though the average particle size is smaller. We chose a specific composition (70:30 SE:AM volume ratio) to provide further insight into the discrepancies between mono- and multimodal distributions and their AM particle size dependence. The tortuosity factor vs. the AM particle size for this composition is shown in Figure S5, Supporting Information. The linear behavior in the log-log plot to the right suggests that power law functions $\tau^2(d) = a \cdot d^{-b}$, with the fit parameters a and b can be used to acquire reasonable fits with the data sets. The fits indicate that the upper limit of the tortuosity factor, which would be reached for vanishing AM particle size, is at a tortuosity factor of $\lim_{d \rightarrow 0 \mu\text{m}} \{\tau_{\text{mono}}^2(d)\} = 6.40$ for a monomodal AM particle distribution and at $\lim_{d \rightarrow 0 \mu\text{m}} \{\tau_{\text{tri}}^2(d)\} = 5.55$ for the chosen group of trimodal distributions at 15 % void space and 70:30 AM:SE volume fraction. We conclude that in comparison to monomodal AM particles, the trimodal particle size distribution reduces ionic tortuosity in this case.

Targeting an ionic tortuosity factor of 3.5, both distributions, mono- and multimodal, require an AM particle size of 12 μm .

(a)



(b)



(c)

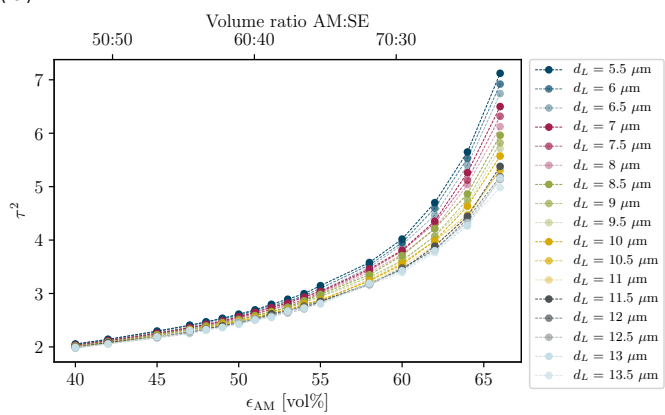


Figure 3: (a) Multimodal particle size distributions for AM with resulting electronic conduction clusters at 55 vol% AM fraction, (b) effective ionic conductivity (c) the ionic tortuosity factor of composite microstructures vs. the fraction of active material for trimodally distributed AM; particle sizes of the largest particles vary linearly between $d_L \in [5.5, 13.5] \mu\text{m}$; medium and small particle's size is held constant at $d_M = 5.5 \mu\text{m}$ and $d_S = 3 \mu\text{m}$, while the electrode void space is held constant at $\phi = 15 \%$.

3.1.5 Electrode void space

Even when fabricated thoroughly, ASSB electrodes exhibit void space that, in contrast to conventional electrodes, cannot be easily penetrated by the (solid) electrolyte. This additional characteristic is rarely thought of, even though there is evidence that it has a strong effect on the conduction properties^{21,26}: Utilizing FIB/SEM reconstruction of a pressed composite cathode of LiNbO₃-coated LCO and amorphous Li₂S-P₂S₅-LiI, Hlushkou et al.²⁶ found 13.2 % of void space coupled with an ionic tortuosity factor of 1.6 and 1.74 by Electrochemical Impedance Spectroscopy (EIS) and simulation in a random-walk particle-tracking technique, respectively. To impart an impression on the impact of void space, they compared the reconstructed microstructure to a fictitious electrode, in which all voids were filled with SE, and found a significantly reduced tortuosity factor of 1.27 in the simulation.

Figure 4 displays the effective ionic conductivity and tortuosity factor vs. the AM:SE volume ratio for void spaces between 5 % and 20 % with 5 μm -sized AM particles. Volume ratios with AM content above 73:27 AM:SE are challenging to obtain in microstructures of 5 % void space, because the limit of dense packing of spheres applies to the AM volume fraction in the entire volume, not to the fraction related to the solid volume ν_{AM} . As observed before, the effective ionic conductivity decreases upon introduction of higher AM fractions for all void spaces. Furthermore, it is evident that a higher void space significantly lowers ionic conductivity, with 2-fold higher effective conductivities for 5 % void space, compared to 20 %. This originates in the loss of ionic pathways in the cathode, when more voids are present. Towards higher AM loading, the effective ionic conductivity drops and the tortuosity factor steeply increases. Since the crucial effect of void space on electronic and ionic conduction clusters and the specific surface area between the two clusters has been reported²¹, we like to emphasize that void space is indeed an important and inherent electrode property which should not be neglected.

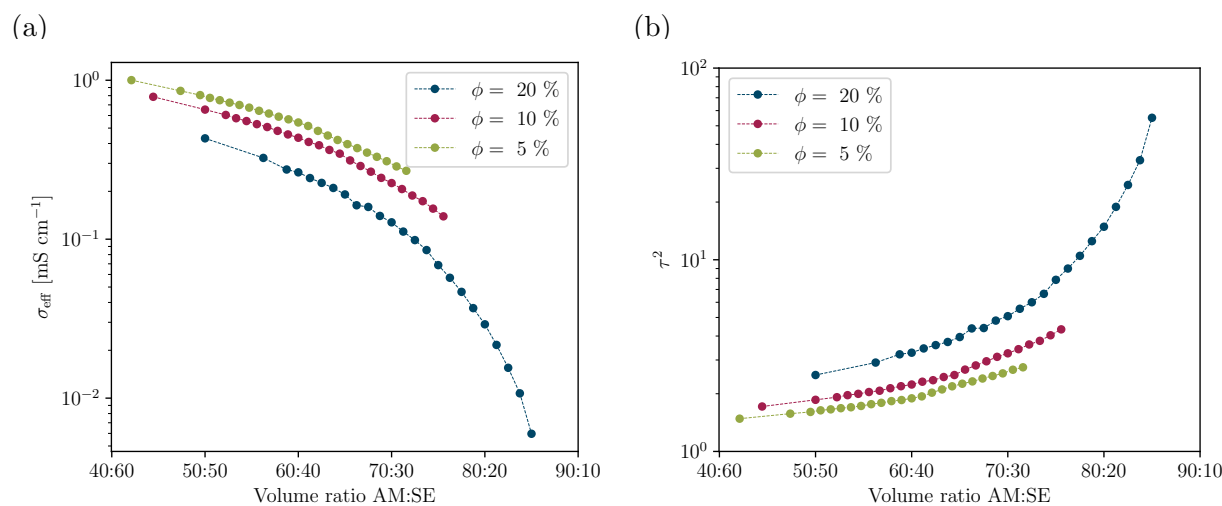


Figure 4: (a) Effective ionic conductivity and (b) ionic tortuosity factor of composite microstructures vs. AM:SE volume ratio for uniformly distributed AM and their dependence on void space at an AM particle size of $d = 5 \mu\text{m}$.

3.2 Binder

Studies of conventional battery electrodes used EIS⁴⁷ or tomography data and simulation⁴⁸ to show that binders can significantly change effective conduction properties. However, since the binder morphology is usually not properly resolved in tomography data⁴⁹, it is challenging to quantify and to understand the effects. To provide insight into the impact of binder in ASSB cathodes, we conducted a binder study evaluating the active surface area between SE and AM, the effective ionic conductivity and the associated ionic tortuosity factor. The volumetric binder fraction was hereby linked to the fraction of AM in the electrode and is denoted by $V(\text{B}) : V(\text{AM})$, which implies that the binder content in wt% is not constant with changing composition, but increases slightly with AM content. As binder materials exhibit quite different gravimetric densities, we calculated the associated binder weight fractions for polyvinylidene difluoride (PVDF) ($\rho_{\text{PVDF}} = 1.78 \text{ g cm}^{-3}$ ⁶⁵) and NBR ($\rho_{\text{NBR}} = 1 \text{ g cm}^{-3}$ ⁶⁶) exemplarily and display them in Figure 5a: The fact that $V(\text{NBR}) : V(\text{AM}) = 0.1$ equals weight fractions lower than 2 wt% for NBR, already indicates that even small binder weight fractions consume significant volume and can therefore critically influence cell performance.

3.2.1 Percolation study

Analogous to our previous work²¹, we identified ionic and electronic conduction networks in the model microstructures. The fraction of AM or SE in the conductive network, the so-called utilization level, is shown for varying AM:SE volume ratio in Figure 5b. Owing to the mechanism of binder generation that was used on an existing AM microstructure, the utilization level of AM is not affected by the presence of binder, but there is a significant effect on the SE utilization for compositions with AM-content larger than in the 70:30 AM:SE volume ratio. We observed ionic limitation for binder-free microstructures in our previous study as well, in particular when voids occupy more space in the electrode²¹. The incorporation of binder impairs this effect: The binder impedes and blocks ionic pathways in the microstructure, hence not all SE particles contribute to ionic conduction.

This can also be observed in the specific active surface area $A_{spec,a}$ in Figure 5c, which is reduced for both binder contents and decreases for compositions with more than 65 vol% AM. Figure 5d shows the same data, normalized to the specific active surface area of binder-free microstructures. The available interface for lithium insertion is reduced by at least 17 % for the smaller binder content and 29 % for the larger binder content in the case of low AM-fractions. For high AM fractions, the reduction even amounts to 43 % and 82 %, respectively. The effect on the cell performance can thus be crucial. In a study on NCM622:LPSCl:C65:NBR-composites, Nam et al.²⁵ obtained lower capacity and rate capability for slurry-processed electrodes than for binder-free dry-mixed electrodes. To gain insight on the AM/SE contact area, Nam et al.²⁵ performed galvanostatic intermittent titration technique (GITT) measurements on half-cells and correlated the contact area to N₂ adsorption-desorption isotherm experiments on NCM622 powders. In their study, the binder content in the slurry-mixed electrodes was held constant at 1.4 wt % for all compositions, corresponding to around 10 vol% NBR:NCM622 in the model microstructures. The experimental data on AM/SE surface area is incorporated in Figure 5d and it is obvious that for the small (70 wt% \simeq 48 vol%) and the large AM fraction (85 wt% \simeq 69 vol%), data and

model match quite well. The intermediate AM:SE composition exhibits better contact than predicted by our model, a fact that Nam et al.²⁵ do not comment on, either. We are aware that a direct comparison is difficult, because not all microstructure-determining properties of the composites are known: The void space may have significant influence on the active surface area and is possibly inherently different between experiment and simulation as well as between the dry- and wet-processed electrodes. Moreover, the AM and SE particle sizes and distributions are unknown and only the AM particle size can be estimated from field-emission scanning electron microscopy surface images²⁵ to be around 5 μm . Another aspect is the presence of C65, a carbon additive that naturally provides high surface area due to its small particle size. Therefore, it blocks parts of the AM surface and can reduce the overall interface area between SE and AM. Finally, experimental results obtained by GITT measurements have shown to be subject to large errors⁶⁷.

3.2.2 Effective conduction

Beyond that, the influence of binder is also predominant in the effective ionic conductivity and the ionic tortuosity factor, as shown in Figure 5e and 5f. While the binder impedes the effective ionic conduction for all compositions, it becomes especially crucial in high energy cells with more AM than in the volume ratio of 70:30 AM:SE+B. In these cases, the conductivity drops abruptly and the ionic tortuosity increases steeply, indicating that ionic transport becomes critical. We like to highlight, that although this effect is enhanced for the higher binder content, it is in general also observable for the small binder content. We expect that this tendency will hold for even higher binder amounts and lead to impaired properties in these cases.

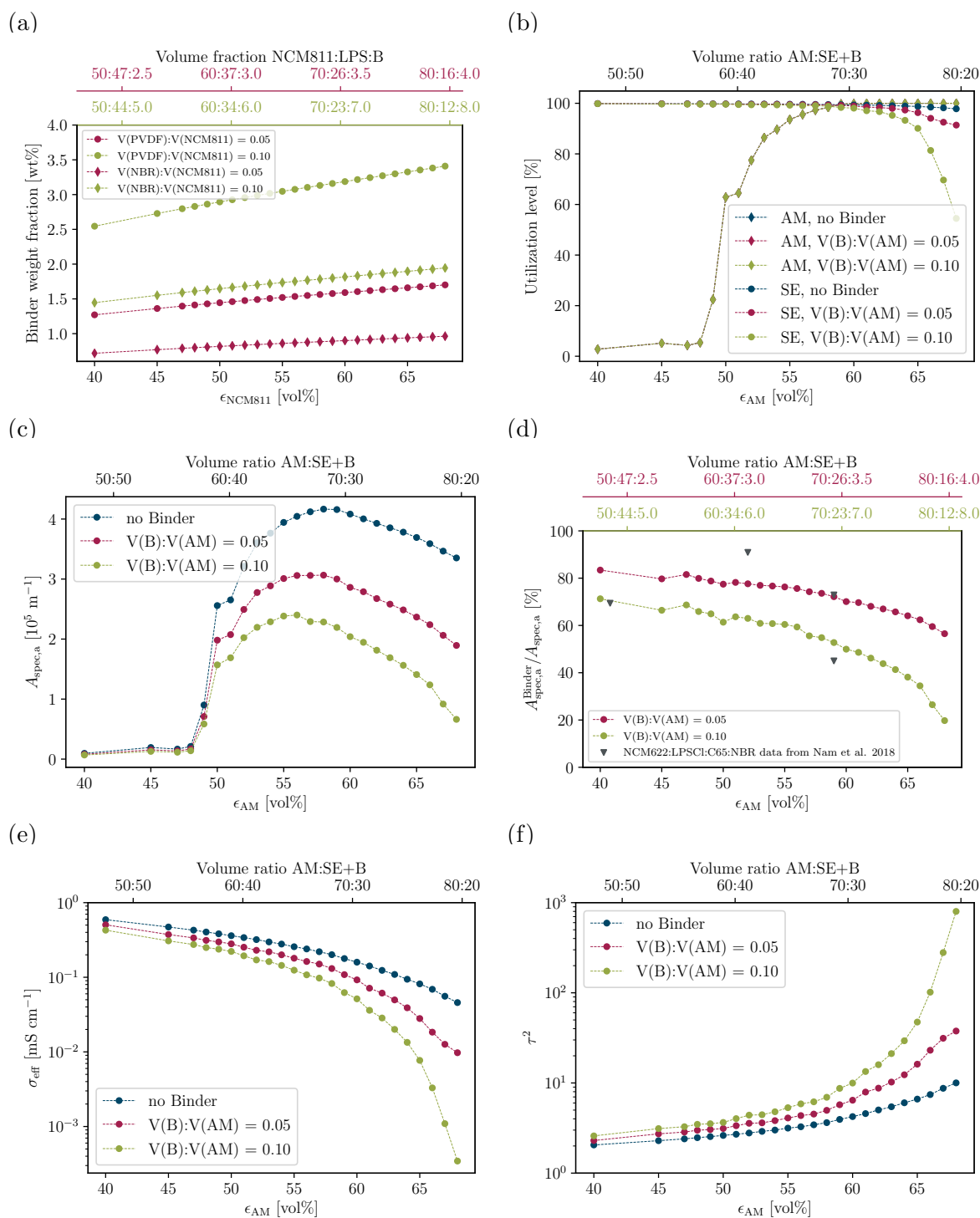


Figure 5: Influence of two different binder fractions on (a) binder weight fraction for PVDF and NBR in NCM811:LPS composites, (b) utilization level of AM and SE (c) active interface area between conductive clusters, (d) relative active interface area (normalized to values of binder-free electrodes), blue points represent data from GITT experiments on NCM622:LPSCI:C65:NBR, reported by Nam et al.²⁵, (e) effective ionic conductivities and (f) ionic tortuosity factors in composite microstructures vs. AM:SE+B (Binder) volume ratio. For the simulation, the AM particle size is $d = 5 \mu\text{m}$ and the electrode void space is constant at $\phi = 15 \%$.

3.3 Applicable current densities

As we gained a better understanding of the different aspects that can influence or impede ionic conduction, the next step is to link these insights to ASSB application and to discuss the influence of microstructure on performance. The approach of estimating the practical current density in different cathode microstructures is basic and relies exclusively on ionic, Ohmic losses.

We calculated the current density according to Equation 15 and show its dependence on electrode thickness, SE bulk conductivity, AM:SE composition and ionic tortuosity in Figures 6a and 6b. As before, a void space of 15 % is assumed, and we used NCM811 with a specific capacity of 196 mA h g^{-1} and a gravimetric density of 4.76 g cm^{-3} to compute the associated C-rates from Equation 17 and display them in Figures 6c and 6d. We restricted the allowed voltage drop ΔU to 0.1 V, as the focus was not on high current pulses, where increased overpotential is commonly accepted, but on a stable and healthy usage. Of course, the current is linearly dependent on the voltage drop (Equation 15), and higher current values can be calculated when higher voltage drops are tolerated. But one should also keep in mind that the ionic, Ohmic loss is not the only contribution: In the assessment of ASSB cathodes, charge-transfer at the interfaces and Li-diffusion within the AM are important aspects that may limit electrode performance, as well. Consequently, our calculation should rather be considered a good case scenario, because interface kinetics and AM diffusion limitation can become crucial for cell performance, even though the effective ionic conduction through the composite may be sufficient. Apart from that, the entire cell can be understood as a series of anode, separator and cathode impedance⁵².

Figure 6a illustrates the effect of electrode thickness and ionic bulk conductivity on the estimated current density for an AM to SE volume fraction of 70:30 and an ionic tortuosity factor of 4, similar to conventional cathodes⁴⁷. It indicates that common SEs, with conductivities below 5 mS cm^{-1} , are not necessarily enablers for thick electrode designs. Instead, highly conductive SE materials are needed for thick electrodes. Thus, when targeting a cur-

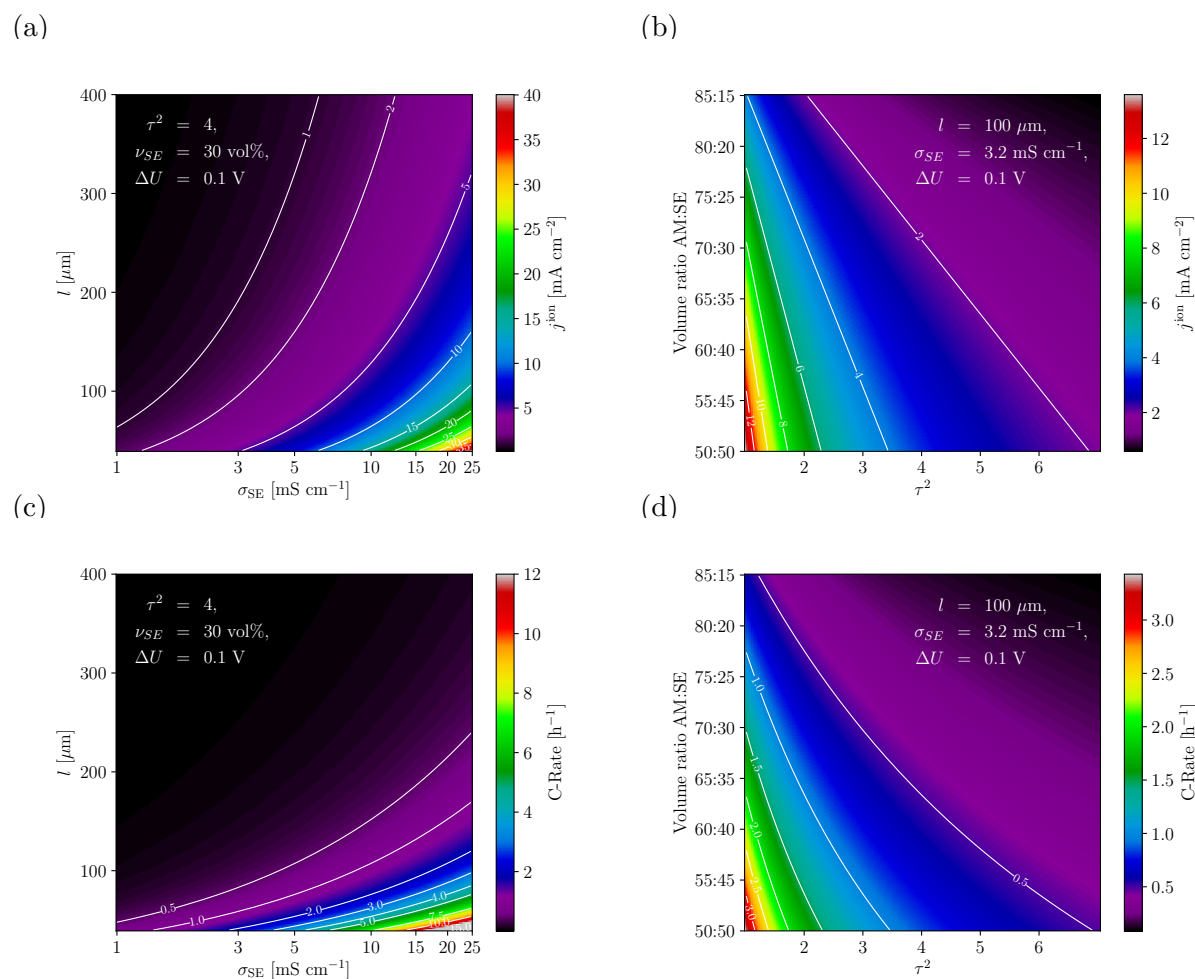


Figure 6: Estimated current densities depending on (a) electrode thickness and SE ionic bulk conductivity and (b) AM:SE composition and ionic tortuosity factor. Resulting C-rates for NCM811 for varying (c) electrode thickness and SE ionic bulk conductivity and (d) AM:SE composition and ionic tortuosity factor, assuming NCM811 and 15 vol% void space.

rent density of 5 mA cm⁻², electrodes thinner than 70 μm are required for a SE with ionic bulk conductivity of 5 mS cm⁻¹. This effect is even more pronounced, when considering the C-rate in Figure 6c, which depends quadratically on the electrode thickness. In this case, an electrode thickness of 100 μm does not allow C-rates above 2 C for SEs with an ionic conductivity below 17 mS cm⁻¹.

Figure 6b shows the influence of composition and ionic tortuosity on the applicable current density for LGPS as a common SE with 3.2 mS cm⁻¹⁴⁴ at 100 μm electrode thickness, suggesting two ways to compensate insufficient SE bulk conductivity when targeting a certain

current density: The usage of higher SE fractions in the electrode or the tuning of the ionic tortuosity. While the first approach counteracts the high capacity, targeted by a thick electrode setup, we previously showed that the ionic tortuosity factor can be influenced by the AM particle size, electrode composition, void space and binder content: Actually, large SE fractions in the composite are likely to involve a reduction of ionic tortuosity (Figure 2), as the amount of AM obstacles in the ionic pathway decreases. The translation into C-rates in Figure 6d highlights that the tortuosity can indeed be a determining electrode characteristic for electrode design, since even for relatively high SE fractions in the composite (45 vol% SE), ionic tortuosity factors above 3 do not allow C-rates higher than 1 C. To analyze the influence of binder, we have to reconsider Figure 5f: The tortuosity, τ^2 , is likely to reach values of 10 for the higher and 6.4 for the lower binder content, respectively, at a composition of 70 vol% AM and 15 % void space. In a NMC811:LPS:NBR composite, this corresponds to 1.8 and 0.9 wt% NBR, respectively (Figure 5a). Compared to a tortuosity of 4.2 in the binder-free microstructure, this discrepancy illustrates that even small binder contents can adversely affect the tortuosity. For the electrode performance, this implies that the applicable current density for 1.8 wt% NBR is at 0.82 mA cm^{-2} (0.15 C), 0.9 wt% NBR suggests 1.3 mA cm^{-2} (0.23 C) and even the binder-free composite exhibits a current density below 2 mA cm^{-2} (0.35 C).

In order to assess, what this means for ASSB application, we further estimated the current density for LGPS and the highly conductive $\text{Li}_{9.54}\text{Si}_{1.74}\text{P}_{1.44}\text{S}_{11.7}\text{Cl}_{0.3}$ (LSiPSCl) with 25 mS cm^{-1} ⁴ and distinguished between three use cases: an energy-driven electrode layout, a high-power cathode and an intermediate setup. The specifications as well as the resulting current densities and C-rates can be found in Table 1. For the high-energy cathode, dense packing of AM particles is essential, so we assumed a thick electrode and a high AM fraction of 80 vol%, which leads to increased tortuosity factors around 10, depending on the particle size (Figures 1-3 and S5), residual void space (Figure 4) and the binder content (Figure 5). The power-based electrode was thinner and featured a higher SE fraction. We referred to

the Bruggeman equation to estimate its lower tortuosity limit. The intermediate cathode possesses a tortuosity of 4, as previously, and a medium thickness.

The applicable current densities for LGPS are quite low for the high-energy and the intermediate case, with C-rates far below 0.2 C. Only the high-power setup would allow for 1.5 C, when a potential drop of 0.1 V is accepted. This highlights the strong influence of the cathode layout and its associated microstructure: A thick, tortuous electrode reaches its limit in ionic conductivity already at small current densities and is therefore inappropriate for fast (dis-)charging, revealing that the trade-off energy vs. power density is not restricted to conventional Li-ion cells. Even though, the current density in the high-power layout is clearly higher, the absolute value of 1.5 C is also not convincing and points out the importance of bulk ionic conductivity for the SE. In comparison to LGPS, the fast-ion conductor LSiPSCl enables enhanced current densities, albeit the high-energy layout is still ionically limited to currents below C/10. This stresses, that apart from material conductivity, microstructural tuning is essential for an energy-optimized electrode design. The choice of particle sizes, size distributions and morphologies of the AM and SE should be considered as important as the SE material conductivities. Furthermore, we like to emphasize that processing is another key driver, because it determines the residual void space, the binder content and its distribution. The case study and Figure 6a in particular suggest that lithium ion conductivities of 10 mS cm^{-1} should be targeted in materials design to achieve good performance at enhanced C-rates and reasonable energy density. In their electrochemical simulation of a garnet-based ASSB full

Table 1: Application cases

			high energy	intermediate	high power
electrode thickness	l	$[\mu\text{m}]$	300	140	100
AM:SE volume fraction	$\nu_{\text{AM}}/\nu_{\text{SE}}$		80:20	70:30	60:40
ionic tortuosity factor	τ^2		10	4	1.7
current density, LGPS	$j_{\text{LGPS}}^{\text{ion}}$	$[\text{mA cm}^{-2}]$	0.18	1.46	7.25
current density, LSiPSCl	$j_{\text{LSiPSCl}}^{\text{ion}}$	$[\text{mA cm}^{-2}]$	1.42	11.4	56.7
C-rate, LGPS	C_{LGPS}	$[\text{h}^{-1}]$	0.010	0.19	1.5
C-rate, LSiPSCl	C_{LSiPSCl}	$[\text{h}^{-1}]$	0.074	1.46	11.9

cell Finsterbusch et al.⁴³ find that an ionic SE conductivity of 2 mS cm^{-1} is sufficient to be par with lithium ion batteries containing a liquid electrolyte for a $50 \text{ }\mu\text{m}$ thick composite cathode at a rate of 1 C. However, for an increased electrode thickness of $100 \text{ }\mu\text{m}$ they observe transport limitations in the SE with 2 mS cm^{-1} which significantly affect the discharge curves and the cell capacity. As these limitations do not occur for a SE conductivity of 11 mS cm^{-1} , we are confident that the evaluation is consistent with our model and the resulting estimate of current densities.

In liquid electrolytes, the ionic conductivity is in the range of $5 - 10 \text{ mS cm}^{-1}$ (at room temperature) depending on the electrolyte system, the salt concentration and the temperature⁶⁸. However, liquid electrolytes are not single-ion conductors and the migration current is carried by lithium ions and the corresponding salt anions (commonly PF_6^-). Therefore, the cationic transference number, used to describe the current fraction carried by the lithium ions, has to be considered. In the case of 1M LiPF_6 at 20°C a typical transference number is 0.27^{68} , implying a maximum partial lithium ion conductivity of 2.7 mS cm^{-1} . So why does our assessment suggest that SEs require a higher ionic conductivity? The essential difference is that the SE does not easily wet the AM surface, but introduces its own microstructure into the electrode with void space and binder strongly affecting (and impeding) ionic pathways. In any case, the production of high-performance ASSB will require advanced processing on all levels of materials, electrodes and cells.

4 Conclusions

For a fundamental understanding of the interdependencies between cathode design, processing and performance, we set up a microstructural modeling procedure for ASSB cathodes, featuring SE, AM and binder. Focusing on the effective ionic conductivity and its associated ionic tortuosity, we studied the influence of AM particle size and distribution, residual void space and binder content. The calculation of the effective ionic conductivity was done in a

flux-based approach on a 3D voxel-microstructure. We eventually presented the trade-offs and showed that application-based design starts at the microstructure level.

The choice of AM particle size can be seen as a trade-off between ionic and electronic conduction: While small AM particles have shown to offer high surface area and good electronic percolation properties^{21,23} as well as short lithium diffusion paths within the AM, in accordance to Froboese et al.²⁷ we point out that they also impede ionic conduction and lead to tortuous pathways for mono- and multimodal size distributions. The electronic percolation issue could be solved by adding conductive carbon or by the usage of high AM fractions, if degradation reactions at the SE/AM and the carbon/SE interfaces are prevented by coating^{10,17,19,29}. To control the ionic tortuosity, while maintaining short diffusion paths within the AM, a sophisticated multimodal particle size distribution can be useful. Furthermore, experimentalists should consider moving on to single crystal AM instead of secondary particles, as these offer different morphologies and small particle sizes^{57,69,70}, connected with smaller surface to bulk ratio, and therefore reduced area for decomposition between AM and SE.

Since it is commonly used in the context of battery electrodes, we compared our results of ionic tortuosity to the Bruggeman relation for spherical particles and found that it is not valid for complex ASSB microstructures and significantly underestimates the tortuosity. Even though the modified Bruggeman relation could be fit to the data, we want to raise awareness that the Bruggeman equation(s) should be used cautiously.

The residual void space and the binder content are two processing-rooted properties, which critically influence ionic transport and the active surface area available for Li-insertion. They are therefore essential for electrode performance, highlighting the importance of large-scale processing that either minimizes the binder amount^{32,34} or incorporates an ion-conductive binder³¹ and reduces void space.

Finally, we demonstrated that the current densities that can be realized in a composite cathode, are strongly dependent on the microstructure and the electrode layout.

Generally, a model microstructure can only be understood as the snapshot of a real ASSB cathode, because the latter are time-variant and influenced by mechanical and chemical effects during cycling³⁰ and aging. Accordingly, future work on the cathode microstructure should focus on elastic modeling and the effects of volume changes, as well as on a full electrochemical simulation, which has the potential to shed light on the impact of microstructure heterogeneities arising from processing or aging and to show how bottlenecks in ion transport develop.

Acknowledgement

The authors thank Volkswagen AG for the financial support of this work. Jürgen Janek thanks the German Federal Ministry of Education and Research (BMBF) for funding within the Cluster of Competence "FESTBATT" (03XP0177A). The authors acknowledge helpful discussion with Philipp Minnmann (JLU) and thank the Math2Market-team for supporting us with a smart script to accurately meet the binder content.

Supporting Information Available

The following files are available free of charge.

Supporting Information: Explanation and scheme of binder generation procedure; modeling parameters for flux-based simulation; scheme of elements for current density estimation; reconstruction of microstructure from Kato et al.⁴⁴; SEM image comparison, overview of modeling parameters; comparison of tortuosity dependence on active material particle size for mono- and trimodal particle size distribution

References

- (1) Hawley, W. B.; Li, J. Electrode Manufacturing for Lithium-Ion Batteries—Analysis of Current and Next Generation Processing. *Journal of Energy Storage* **2019**, *25*, 100862.
- (2) Luntz, A. C.; Voss, J.; Reuter, K. Interfacial Challenges in Solid-State Li Ion Batteries. *J. Phys. Chem. Lett.* **2015**, *6*, 4599–4604.
- (3) Zhu, G.-L.; Zhao, C.-Z.; Huang, J.-Q.; He, C.; Zhang, J.; Chen, S.; Xu, L.; Yuan, H.; Zhang, Q. Fast Charging Lithium Batteries: Recent Progress and Future Prospects. *Small* **2019**, *15*, 1805389.
- (4) Kato, Y.; Hori, S.; Saito, T.; Suzuki, K.; Hirayama, M.; Mitsui, A.; Yonemura, M.; Iba, H.; Kanno, R. High-Power All-Solid-State Batteries using Sulfide Superionic Conductors. *Nature Energy* **2016**, *1*, 16030.
- (5) Schnell, J.; Günther, T.; Knoche, T.; Vieider, C.; Köhler, L.; Just, A.; Keller, M.; Passerini, S.; Reinhart, G. All-Solid-State Lithium-Ion and Lithium Metal Batteries – Paving the Way to Large-Scale Production. *Journal of Power Sources* **2018**, *382*, 160–175.
- (6) Zhang, Z.; Shao, Y.; Lotsch, B.; Hu, Y.-S.; Li, H.; Janek, J.; Nazar, L. F.; Nan, C.-W.; Maier, J.; Armand, M.; Chen, L. New Horizons for Inorganic Solid State Ion Conductors. *Energy Environ. Sci.* **2018**, *11*, 1945–1976.
- (7) Culver, S. P.; Koerver, R.; Krauskopf, T.; Zeier, W. G. Designing Ionic Conductors: The Interplay between Structural Phenomena and Interfaces in Thiophosphate-Based Solid-State Batteries. *Chem. Mater.* **2018**, *30*, 4179–4192.
- (8) Dewald, G.; Ohno, S.; Kraft, M.; Koerver, R.; Till, P.; Vargas, N.; Janek, J.; Zeier, W. Experimental Assessment of the Practical Oxidative Stability of Lithium Thiophosphate Solid Electrolytes. 2019; <https://doi.org/10.26434/chemrxiv.8014715.v1>.

- (9) Krauskopf, T.; Hartmann, H.; Zeier, W. G.; Janek, J. Toward a Fundamental Understanding of the Lithium Metal Anode in Solid-State Batteries—An Electrochemical Mechanical Study on the Garnet-Type Solid Electrolyte $\text{Li}_{6.25}\text{Al}_{0.25}\text{La}_3\text{Zr}_2\text{O}_{12}$. *ACS Appl. Mater. Interfaces* **2019**, *11*, 14463–14477.
- (10) Wang, C. et al. Manipulating Interfacial Nanostructure to Achieve High-Performance All-Solid-State Lithium-Ion Batteries. *Small Methods* **2019**, *3*, 1900261.
- (11) Dietrich, C.; Koerver, R.; Gaultois, M. W.; Kieslich, G.; Cibin, G.; Janek, J.; Zeier, W. G. Spectroscopic Characterization of Lithium Thiophosphates by XPS and XAS – A Model to Help Monitor Interfacial Reactions in All-Solid-State Batteries. *Phys. Chem. Chem. Phys.* **2018**, *20*, 20088–20095.
- (12) de Klerk, N.; Wagemaker, M. Space-Charge Layers in All-Solid-State Batteries; Important or Negligible? *ACS Applied Energy Materials* **2018**, *1*, 5609–5618.
- (13) Yamamoto, K.; Iriyama, Y.; Asaka, T.; Hirayama, T.; Fujita, H.; Fisher, C. A. J.; Nonaka, K.; Sugita, Y.; Ogumi, Z. Dynamic Visualization of the Electric Potential in an All-Solid-State Rechargeable Lithium Battery. *Angewandte Chemie International Edition* **2010**, *49*, 4414–4417.
- (14) Haruyama, J.; Sodeyama, K.; Han, L.; Takada, K.; Tateyama, Y. Space-Charge Layer Effect at Interface between Oxide Cathode and Sulfide Electrolyte in All-Solid-State Lithium-Ion Battery. *Chem. Mater.* **2014**, *26*, 4248–4255.
- (15) Ito, S.; Fujiki, S.; Yamada, T.; Aihara, Y.; Park, Y.; Kim, T. Y.; Baek, S.-W.; Lee, J.-M.; Doo, S.; Machida, N. A Rocking Chair Type All-Solid-State Lithium Ion Battery Adopting Li_2O – ZrO_2 Coated $\text{LiNi}_{0.8}\text{Co}_{0.15}\text{Al}_{0.05}\text{O}_2$ and a Sulfide Based Electrolyte. *Journal of Power Sources* **2014**, *248*, 943–950.
- (16) Xiao, Y.; Miara, L. J.; Wang, Y.; Ceder, G. Computational Screening of Cathode Coatings for Solid-State Batteries. *Joule* **2019**, *3*, 1252–1275.

- (17) Culver, S. P.; Koerver, R.; Zeier, W. G.; Janek, J. On the Functionality of Coatings for Cathode Active Materials in Thiophosphate-Based All-Solid-State Batteries. *Advanced Energy Materials* **2019**, *9*, 1900626.
- (18) Nakamura, T.; Amezawa, K.; Kulisch, J.; Zeier, W. G.; Janek, J. Guidelines for All-Solid-State Battery Design and Electrode Buffer Layers Based on Chemical Potential Profile Calculation. *ACS Appl. Mater. Interfaces* **2019**, *11*, 19968–19976.
- (19) Li, X. et al. Unravelling the Chemistry and Microstructure Evolution of a Cathodic Interface in Sulfide-Based All-Solid-State Li-Ion Batteries. *ACS Energy Lett* **2019**, *4*, 2480–2488.
- (20) Keller, M.; Varzi, A.; Passerini, S. Hybrid Electrolytes for Lithium Metal Batteries. *Journal of Power Sources* **2018**, *392*, 206–225.
- (21) Bielefeld, A.; Weber, D. A.; Janek, J. Microstructural Modeling of Composite Cathodes for All-Solid-State Batteries. *J. Phys. Chem. C* **2019**, *123*, 1626–1634.
- (22) Park, J.; Kim, D.; Appiah, W. A.; Song, J.; Bae, K. T.; Lee, K. T.; Oh, J.; Kim, J. Y.; Lee, Y.-G.; Ryou, M.-H.; Lee, Y. M. Electrode Design Methodology for All-Solid-State Batteries: 3D Structural Analysis and Performance Prediction. *Energy Storage Materials* **2019**, *19*, 124–129.
- (23) Strauss, F.; Bartsch, T.; de Biasi, L.; Kim, A.-Y.; Janek, J.; Hartmann, P.; Brezesinski, T. Impact of Cathode Material Particle Size on the Capacity of Bulk-Type All-Solid-State Batteries. *ACS Energy Letters* **2018**, *3*, 992–996.
- (24) Siroma, Z.; Sato, T.; Takeuchi, T.; Nagai, R.; Ota, A.; Ioroi, T. AC Impedance Analysis of Ionic and Electronic Conductivities in Electrode Mixture Layers for an All-Solid-State Lithium-Ion Battery. *Journal of Power Sources* **2016**, *316*, 215–223.

- (25) Nam, Y. J.; Oh, D. Y.; Jung, S. H.; Jung, Y. S. Toward Practical All-Solid-State Lithium-Ion Batteries with High Energy Density and Safety: Comparative Study for Electrodes Fabricated by Dry- and Slurry-Mixing Processes. *Journal of Power Sources* **2018**, *375*, 93–101.
- (26) Hlushkou, D.; Reising, A. E.; Kaiser, N.; Spannenberger, S.; Schlabach, S.; Kato, Y.; Roling, B.; Tallarek, U. The Influence of Void Space on Ion Transport in a Composite Cathode for All-Solid-State Batteries. *Journal of Power Sources* **2018**, *396*, 363–370.
- (27) Froboese, L.; van der Sichel, J. F.; Loellhoeffel, T.; Helmers, L.; Kwade, A. Effect of Microstructure on the Ionic Conductivity of an All Solid-State Battery Electrode. *Journal of The Electrochemical Society* **2019**, *166*, A318–A328.
- (28) Shi, T.; Tu, Q.; Tian, Y.; Xiao, Y.; Miara, L. J.; Kononova, O.; Ceder, G. High Active Material Loading in All-Solid-State Battery Electrode via Particle Size Optimization. *Advanced Energy Materials* **2020**, *10*, 1902881.
- (29) Koerver, R.; Aygün, I.; Leichtweiß, T.; Dietrich, C.; Zhang, W.; Binder, J. O.; Hartmann, P.; Zeier, W. G.; Janek, J. Capacity Fade in Solid-State Batteries: Interphase Formation and Chemomechanical Processes in Nickel-Rich Layered Oxide Cathodes and Lithium Thiophosphate Solid Electrolytes. *Chemistry of Materials* **2017**, *29*, 5574–5582.
- (30) Koerver, R.; Zhang, W.; de Biasi, L.; Schweidler, S.; Kondrakov, A. O.; Kolling, S.; Brezesinski, T.; Hartmann, P.; Zeier, W. G.; Janek, J. Chemo-Mechanical Expansion of Lithium Electrode Materials - On the Route to Mechanically Optimized All-Solid-State Batteries. *Energy Environ. Sci.* **2018**, *11*, 2142–2158.
- (31) Oh, D. Y.; Nam, Y. J.; Park, K. H.; Jung, S. H.; Kim, K. T.; Ha, A. R.; Jung, Y. S. Slurry-Fabricable Li⁺-Conductive Polymeric Binders for Practical All-Solid-

- State Lithium-Ion Batteries Enabled by Solvate Ionic Liquids. *Advanced Energy Materials* **2019**, *9*, 1802927.
- (32) Hippauf, F.; Schumm, B.; Doerfler, S.; Althues, H.; Fujiki, S.; Shiratsushi, T.; Tsujimura, T.; Aihara, Y.; Kaskel, S. Overcoming Binder Limitations of Sheet-Type Solid-State Cathodes using a Solvent-Free Dry-Film Approach. *Energy Storage Materials* **2019**, *21*, 390–398.
- (33) Inada, T.; Takada, K.; Kajiyama, A.; Kouguchi, M.; Sasaki, H.; Kondo, S.; Watanabe, M.; Murayama, M.; Kanno, R. Fabrications and Properties of Composite Solid-State Electrolytes. *Solid State Ionics* **2003**, *158*, 275–280.
- (34) Yamamoto, M.; Terauchi, Y.; Sakuda, A.; Takahashi, M. Binder-Free Sheet-Type All-Solid-State Batteries with Enhanced Rate Capabilities and High Energy Densities. *Scientific Reports* **2018**, *8*, 1212.
- (35) Kim, D. H.; Oh, D. Y.; Park, K. H.; Choi, Y. E.; Nam, Y. J.; Lee, H. A.; Lee, S.-M.; Jung, Y. S. Infiltration of Solution-Processable Solid Electrolytes into Conventional Li-Ion-Battery Electrodes for All-Solid-State Li-Ion Batteries. *Nano Letters* **2017**, *17*, 3013–3020.
- (36) Oh, D. Y.; Nam, Y. J.; Park, K. H.; Jung, S. H.; Cho, S.-J.; Kim, Y. K.; Lee, Y.-G.; Lee, S.-Y.; Jung, Y. S. Excellent Compatibility of Solvate Ionic Liquids with Sulfide Solid Electrolytes: Toward Favorable Ionic Contacts in Bulk-Type All-Solid-State Lithium-Ion Batteries. *Advanced Energy Materials* **2015**, *5*, 1500865.
- (37) Oh, D. Y.; Kim, D. H.; Jung, S. H.; Han, J.-G.; Choi, N.-S.; Jung, Y. S. Single-Step Wet-Chemical Fabrication of Sheet-Type Electrodes from Solid-Electrolyte Precursors for All-Solid-State Lithium-Ion Batteries. *J. Mater. Chem. A* **2017**, *5*, 20771–20779.
- (38) Rippa, N.; Strobl, P.; Stiaszny, B.; Zinkevich, T.; Yavuz, M.; Schnell, J.; Indris, S.; Gasteiger, H. A.; Sedlmaier, S. J. Slurry-Based Processing of Solid Electrolytes: A

- Comparative Binder Study. *Journal of The Electrochemical Society* **2018**, *165*, A3993–A3999.
- (39) Math2Market GmbH, K. G. GeoDict — The Digital Material Laboratory, Version 2019 SP 2. 2019.
- (40) Sakuda, A.; Hayashi, A.; Tatsumisago, M. Sulfide Solid Electrolyte with Favorable Mechanical Property for All-Solid-State Lithium Battery. *Scientific Reports* **2013**, *3*, 2261.
- (41) Deng, Z.; Wang, Z.; Chu, I.-H.; Luo, J.; Ong, S. Elastic Properties of Alkali Superionic Conductor Electrolytes from First Principles Calculations. *Journal of The Electrochemical Society* **2016**, *163*, A67–A74.
- (42) Randau, S.; Weber, D. A.; Kötz, O.; Koerver, R.; Braun, P.; Weber, A.; Ivers-Tiffée, E.; Adermann, T.; Kulisch, J.; Zeier, W. G.; Richter, F. H.; Janek, J. Benchmarking the Performance of All-Solid-State Lithium Batteries. *Nature Energy* **2020**, *8*, in print.
- (43) Finsterbusch, M.; Danner, T.; Tsai, C.-L.; Uhlenbruck, S.; Latz, A.; Guillon, O. High Capacity Garnet-Based All-Solid-State Lithium Batteries: Fabrication and 3D-Microstructure Resolved Modeling. *ACS Applied Materials & Interfaces* **2018**, *10*, 22329–22339.
- (44) Kato, Y.; Shiotani, S.; Morita, K.; Suzuki, K.; Hirayama, M.; Kanno, R. All-Solid-State Batteries with Thick Electrode Configurations. *The Journal of Physical Chemistry Letters* **2018**, *9*, 607–613.
- (45) Tjaden, B.; Brett, D. J. L.; Shearing, P. R. Tortuosity in Electrochemical Devices: A Review of Calculation Approaches. *International Materials Reviews* **2018**, *63*, 47–67.
- (46) Landesfeind, J.; Ebner, M.; Eldiven, A.; Wood, V.; Gasteiger, H. A. Tortuosity of

- Battery Electrodes: Validation of Impedance-Derived Values and Critical Comparison with 3D Tomography. *Journal of The Electrochemical Society* **2018**, *165*, A469–A476.
- (47) Landesfeind, J.; Hattendorff, J.; Ehrl, A.; Wall, W. A.; Gasteiger, H. A. Tortuosity Determination of Battery Electrodes and Separators by Impedance Spectroscopy. *Journal of The Electrochemical Society* **2016**, *163*, A1373–A1387.
- (48) Trembacki, B. L.; Mistry, A. N.; Noble, D. R.; Ferraro, M. E.; Mukherjee, P. P.; Roberts, S. A. Editors' Choice—Mesoscale Analysis of Conductive Binder Domain Morphology in Lithium-Ion Battery Electrodes. *Journal of The Electrochemical Society* **2018**, *165*, E725–E736.
- (49) Almar, L.; Joos, J.; Weber, A.; Ivers-Tiffée, E. Microstructural Feature Analysis of Commercial Li-Ion Battery Cathodes by Focused Ion Beam Tomography. *Journal of Power Sources* **2019**, *427*, 1–14.
- (50) Wiegmann, A.; Zemitis, A. EJ-HEAT: A Fast Explicit Jump Harmonic Averaging Solver for the Effective Heat Conductivity of Composite Materials. *Report of the Fraunhofer ITWM* **2006**, *94*.
- (51) Amin, R.; Chiang, Y.-M. Characterization of Electronic and Ionic Transport in $\text{Li}_{1-x}\text{Ni}_{0.33}\text{Mn}_{0.33}\text{Co}_{0.33}\text{O}_2$ (NMC333) and $\text{Li}_{1-x}\text{Ni}_{0.50}\text{Mn}_{0.20}\text{Co}_{0.30}\text{O}_2$ (NMC523) as a Function of Li Content. *Journal of The Electrochemical Society* **2016**, *163*, A1512–A1517.
- (52) Braun, P.; Uhlmann, C.; Weiss, M.; Weber, A.; Ivers-Tiffée, E. Assessment of All-Solid-State Lithium-Ion Batteries. *Journal of Power Sources* **2018**, *393*, 119–127.
- (53) Zielke, L.; Hutzenlaub, T.; Wheeler, D. R.; Chao, C.-W.; Manke, I.; Hilger, A.; Paust, N.; Zengerle, R.; Thiele, S. Three-Phase Multiscale Modeling of a LiCoO₂ Cathode: Combining the Advantages of FIB–SEM Imaging and X-Ray Tomography. *Advanced Energy Materials* **2015**, *5*, 1401612.

- (54) Bauer, W.; Nötzel, D.; Wenzel, V.; Nirschl, H. Influence of Dry Mixing and Distribution of Conductive Additives in Cathodes for Lithium Ion Batteries. *Journal of Power Sources* **2015**, *288*, 359–367.
- (55) Ates, T.; Keller, M.; Kulisch, J.; Adermann, T.; Passerini, S. Development of an All-Solid-State Lithium Battery by Slurry-Coating Procedures using a Sulfidic Electrolyte. *Energy Storage Materials* **2019**, *17*, 204–210.
- (56) Tsai, P.-C.; Wen, B.; Wolfman, M.; Choe, M.-J.; Pan, M. S.; Su, L.; Thornton, K.; Cabana, J.; Chiang, Y.-M. Single-Particle Measurements of Electrochemical Kinetics in NMC and NCA Cathodes for Li-Ion Batteries. *Energy Environ. Sci.* **2018**, *11*, 860–871.
- (57) Li, J.; Li, H.; Stone, W.; Weber, R.; Hy, S.; Dahn, J. R. Synthesis of Single Crystal $\text{LiNi}_{0.5}\text{Mn}_{0.3}\text{Co}_{0.2}\text{O}_2$ for Lithium Ion Batteries. *Journal of The Electrochemical Society* **2017**, *164*, A3529–A3537.
- (58) Ebner, M.; Chung, D.-W.; García, R. E.; Wood, V. Tortuosity Anisotropy in Lithium-Ion Battery Electrodes. *Advanced Energy Materials* **2014**, *4*, 1301278.
- (59) Giesche, H. Mercury Porosimetry: A General (Practical) Overview. *Particle & Particle Systems Characterization* **2006**, *23*, 9–19.
- (60) Bruggeman, D. A. G. Berechnung verschiedener physikalischer Konstanten von heterogenen Substanzen. I. Dielektrizitätskonstanten und Leitfähigkeiten der Mischkörper aus isotropen Substanzen. *Annalen der Physik* **1935**, *416*, 636–664.
- (61) Shen, L.; Chen, Z. Critical Review of the Impact of Tortuosity on Diffusion. *Chemical Engineering Science* **2007**, *62*, 3748–3755.
- (62) Thorat, I. V.; Stephenson, D. E.; Zacharias, N. A.; Zaghbi, K.; Harb, J. N.;

- Wheeler, D. R. Quantifying Tortuosity in Porous Li-Ion Battery Materials. *Journal of Power Sources* **2009**, *188*, 592–600.
- (63) Tóth, L. F., Ed. *Dichteste Kugelpackung. Eine Idee von Gauß*; Abhandlungen der Braunschweigischen Wissenschaftlichen Gesellschaft; Goltze: Göttingen, 1977; Vol. 27.
- (64) Müller, U. *Anorganische Strukturchemie*, 6th ed.; Teubner Studienbücher Chemie; Vieweg+Teubner Verlag: Wiesbaden, 2008.
- (65) Sigma Aldrich, Safety Data Sheet according to Regulation (EC) No. 1907/2006: Poly(vinylidene fluoride). 17.12.2018.
- (66) Sigma Aldrich, Safety Data Sheet according to Regulation (EC) No. 1907/2006: Poly(acrylonitrile-co-butadiene). 17.12.2018.
- (67) Shen, Z.; Cao, L.; Rahn, C. D.; Wang, C.-Y. Least Squares Galvanostatic Intermittent Titration Technique (LS-GITT) for Accurate Solid Phase Diffusivity Measurement. *Journal of The Electrochemical Society* **2013**, *160*, A1842–A1846.
- (68) Landesfeind, J.; Gasteiger, H. A. Temperature and Concentration Dependence of the Ionic Transport Properties of Lithium-Ion Battery Electrolytes. *Journal of The Electrochemical Society* **2019**, *166*, A3079–A3097.
- (69) Li, J.; Cameron, A. R.; Li, H.; Glazier, S.; Xiong, D.; Chatzidakis, M.; Allen, J.; Botton, G. A.; Dahn, J. R. Comparison of Single Crystal and Polycrystalline $\text{LiNi}_{0.5}\text{Mn}_{0.3}\text{Co}_{0.2}\text{O}_2$ Positive Electrode Materials for High Voltage Li-Ion Cells. *Journal of The Electrochemical Society* **2017**, *164*, A1534–A1544.
- (70) Li, H.; Li, J.; Ma, X.; Dahn, J. R. Synthesis of Single Crystal $\text{LiNi}_{0.6}\text{Mn}_{0.2}\text{Co}_{0.2}\text{O}_2$ with Enhanced Electrochemical Performance for Lithium Ion Batteries. *Journal of The Electrochemical Society* **2018**, *165*, A1038–A1045.

TOC Graphic

